Flux Normalisation of the ARGUS Detector at the BGOOD Experiment

Maximilian Pütz

Bachelorarbeit in Physik
angefertigt im Physikalischen Institut

vorgelegt der
Mathematisch-Naturwissenschaftlichen Fakultät
der
Rheinischen Friedrich-Wilhelms-Universität
Bonn

Mai 2024

Ich versichere, dass ich diese Arbeit selbstständig verfasst und keine anderen als die angegebenen Quellen und Hilfsmittel benutzt sowie die Zitate kenntlich gemacht habe.

Bonn, ...

Datum Unterschrift

1. Gutachter: Prof. Dr. Hartmut Schmieden
2. Gutachter: Dr. Thomas Jude

Acknowledgements

I would like to give thanks to Prof. Dr. Schmieden and his group for the support and guidance throughout the completion of this thesis. Special thanks go to Dr. Katrin Kohl who helped me a lot with her ideas and technical knowledge.

Contents

CHAPTER 1

Introduction and Motivation

A core component of research in particle physics is the discovery of the fundamental building blocks of our universe and dates back to the discovery of the electron in the late 19th century.
An important property of particle reactions is the probability of a certain reaction to occur, the so called *cross-section*. In detector experiments aimed at determining cross-sections, a high energy resolution is often a limiting factor and improving it comes often at the expense of other detector characteristics like time resolution. The BGOOD experiment at the University of Bonn aims to investigate meson photoproduction. The experiment combines a BGO-calorimeter with a high resolution forward spectrometer to measure neutral and charged particles. The initial electron beam enters the detector through a radiator, where bremsstrahlung occurs and a photon beam is forwarded to the target inside the detector. The tagging system helps find out the photon energies, with two detectors measuring the momentum of the post-bremsstrahlung electrons. These are: the Tagger, which covers a wide energy range and has a high detection efficiency, or the ARGUS detector, which has better energy resolution but covers a smaller energy range [1].
Until now, only the Tagger has been used to determine cross-sections. The focus of this thesis will be to thoroughly investigate the detection efficiency of ARGUS relative to the Tagger, with the ultimate goal of testing whether a selected cross-section can be correctly determined using the relative ARGUS detection efficiency.

CHAPTER 2

Experimental setup and analysis tools

The BGOOD experiment is located at the ELSA facility. It combines a BGO calorimeter with a forward magnetic spectrometer and a tagging system. Its primary function is to detect neutral and charged particles and to conduct measurements on meson photoproduction, within both the strange and non-strange quark sectors. The experiment is especially suited for processes at low momentum transfer. The following section covers the main components of the BGOOD experiment and is mainly based on the BGOOD technical paper [1].

2.1 ELSA

The ELSA (Electron Stretcher Accelerator) [2] accelerates electrons. An overview of the accelerator setup is shown in Figure 2.1. The acceleration process is divided in three stages. Electrons from a thermal source are initially directed into the LINAC, where they reach an energy of 26 MeV. In the following stage the Booster Synchrotron accelerates the electron beam to an energy of 1.2 GeV. Once the desired energy is achieved, the beam is extracted and transferred to the third stage, the Stretcher Ring. From the Stretcher Ring, the beam can be extracted to the BGOOD experiment.

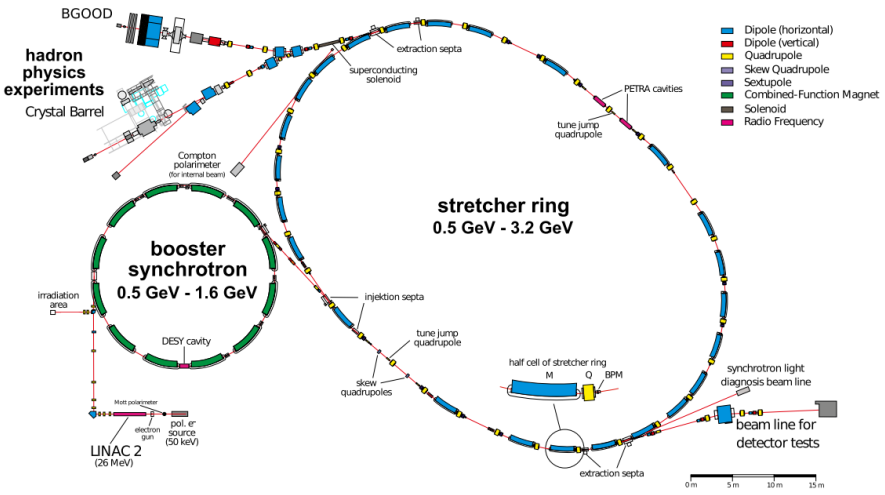

Figure 2.1: Overview of the ELSA accelerator setup [3].

2.2 BGOOD

An overview of the BGOOD experimental setup can be seen in Figure 2.2. The BGOOD tagging system is responsible for determining the energies of the photons that enter the detector by measuring the momentum of the bremsstrahlung electrons. The central detector covers an angular range of close to 4π and is useful for detecting photons and charged particles. In the forward spectrometer, charged particles can be detected with high momentum resolution, in addition to time-of-flight measurements, which allow for precise particle identification.

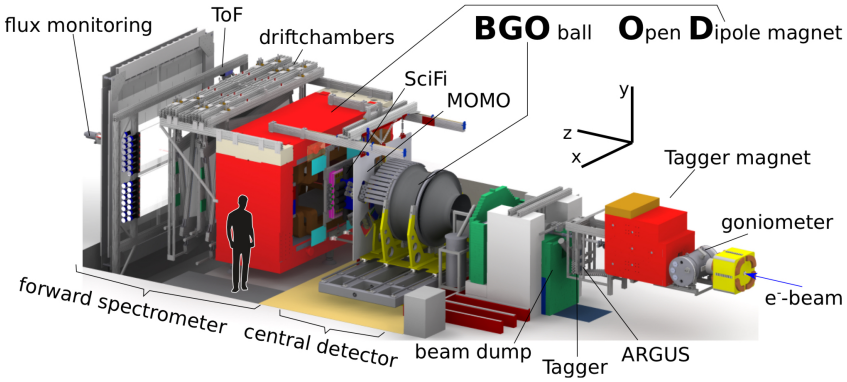

Figure 2.2: Overview of the experimental Setup of the BGOOD experiment [1]

2.2.1 Central detector

The central component of the detector is the BGO calorimeter. The beam enters the BGO calorimeter as illustrated in Figure 2.3. At the core of the detector lies the liquid hydrogen H_2 or deuterium D_2 target, enclosed by the so-called BGO Rugby ball, a cylindrical scintillator barrel, and two MWPCs (multi-wire

proportional chambers). The target is housed within a small aluminium cylinder and positioned in a vacuum tube along the beam path. A scintillator barrel is installed around the target cavity in the beam direction to distinguish between charged and neutral particles produced in the scattering process from the target. Surrounding the center at an angle of $(25 \div 155)^\circ$ is the BGO Rugby Ball. It consists of 480 bismuth germanate (BGO) crystals, divided into 15 sections, each containing 32 crystals. The scintillation crystals are sensitive to both charged and uncharged particles. MOMO[1] and a Scintillator Ring (SciRi), keep track of the direction of charged particles that leave the central detector in the forward direction.

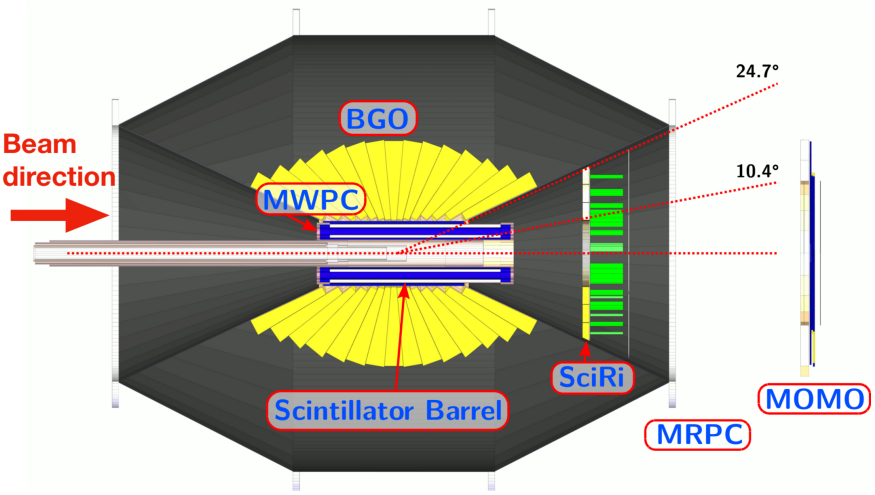

Figure 2.3: Side view of the central detector with the BGO Rugby ball, the scintillator barres, and MOMO and SciRi in forward direction. *BGO Rugby Ball.* The MRPC (Multi-gap Resistive Plate Chamber) is still under construction. Figure adapted from [4].

2.2.2 Forward spectrometer

Behind the BGO rugby ball, the forward spectrometer is installed. An overview of the setup can be found in Figure 2.4. The main purpose of the forward spectrometer is to measure the momentum of charged particles in the very forward direction. Within a polar angle range of $(1 \div 12)^\circ$ an open dipole magnet bends the trajectory of charged particles depending on their momentum and charge. Behind the open dipole magnet, particles are tracked by eight layers of drift chambers. From the curvature of the particle's track, the momentum is determined. The final component of the forward spectrometer is a Time-of-Flight (ToF) spectrometer, which measures the velocity of the incoming particles. In combination with the measured momentum, particles can be identified. MOMO and SciFi, two scintillating fibre tracking detectors, measure the trajectories of charged particles before they enter the magnetic field.

[1] Monitor of Mesonic Observables facility.

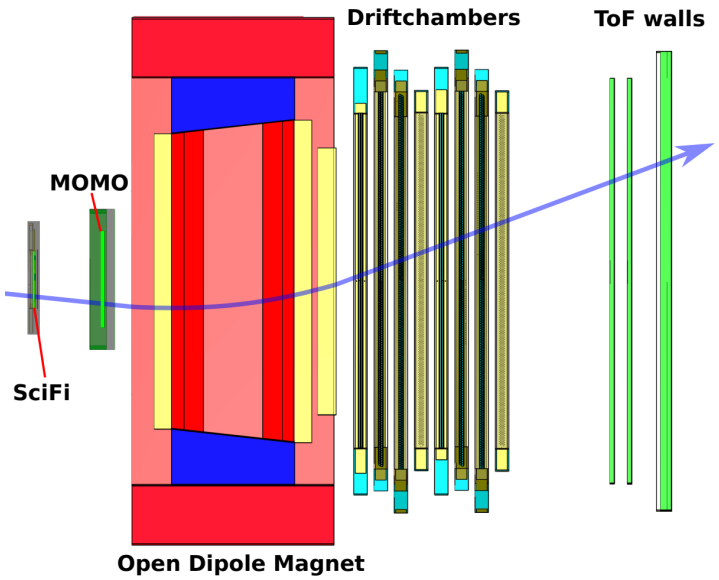

Figure 2.4: Top view of the forward spectrometer, adapted from [5].

2.2.3 Photon tagging system

The photon tagging system in the BGOOD experiment plays an important role, by precisely measuring the energy and time of bremsstrahlung electrons. Coordinating timing coincidences with other detectors enables the correlation of photons with their associated hadronic reactions. An overview of the tagging system is shown in Figure 2.5. When the electron beam hits the radiator, bremsstrahlung occurs, producing a photon spectrum and corresponding bremsstrahlung electrons. The photon beam from the radiator is directed onto the target in the central detector. The electrons are separated from the beam in a magnetic spectrometer and directed onto the ARGUS and tagging hodoscope (Tagger). Here the electron energy E_e is measured, which is directly related to the energy E_γ of the corresponding photon that reaches the target.

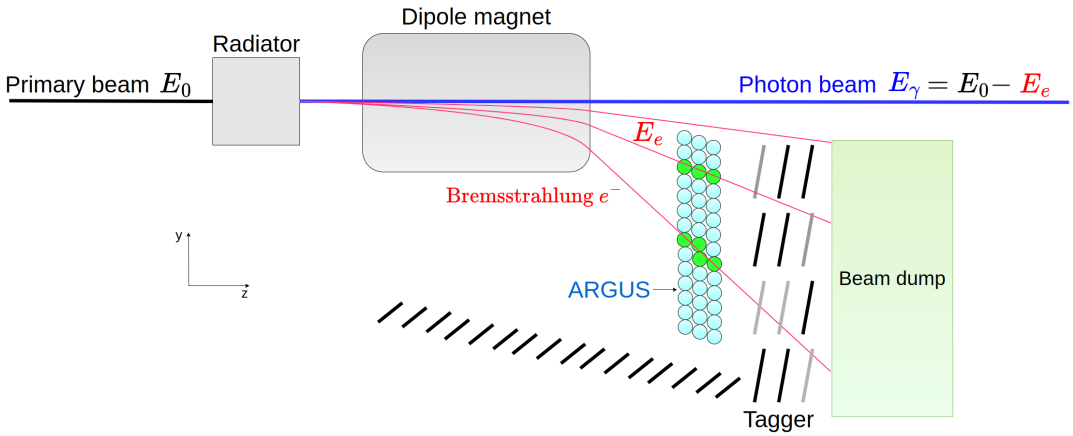

Figure 2.5: Schematic side view of the photon tagging system adapted from [1]. The scale of the tagging hodoscope was adjusted. In practice, the Tagger has a total of 120 scintillator plates and the ARGUS has around 480 scintillation fibers.

Bremsstrahlung Photon Beam and collimator system

The unpolarised electron beam generated by ELSA, with energies of up to 3.2 GeV, is directed onto a radiator inside a goniometer. In the radiator, bremsstrahlung occurs. The deceleration process yields photons across a continuous energy spectrum. The polarisation type depends on the material used in the radiator. For unpolarised photons, amorphous radiators like copper are used, producing incoherent bremsstrahlung with an $1/E_\gamma$ shaped energy spectrum. At the rear end of the tagging system, a setup consisting of two 20 cm long lead collimators and a permanent magnet is installed, to filter out charged particles. Some of the photons produced in the radiator are lost in the collimator system.

Flux monitors

To later determine cross-sections for the reaction channels, it is necessary to know the photon flux that reaches the target, to perform normalisations of collected data. Therefore the photon flux is monitored by two detector components, the so-called FluMo and GIM, which are placed at the very end of the BGOOD experiment. Together with the photon tagging system, they determine the likelihood $P_\gamma(E_\gamma)$, for a photon produced in the radiator to reach the target. More about the Flux monitors can also be read in [5, p.15].

Magnetic spectrometer and tagging hodoscope

After the bremsstrahlung process, the decelerated bremsstrahlung electrons encounter a magnetic field generated by a dipole magnet, as depicted in Figure 2.5. The electrons are directed towards the tagging hodoscope, where their positions are measured. The tagging hodoscope consists of plastic scintillators covering an energy range from 10% to 90% of the incoming electron beam. A total of 54 scintillators are aligned horizontally and 66 vertically to the incoming beam. A detailed view of the tagging hodoscope, including the physical widths of the plastic scintillators, is presented in Figure 2.6. The physical widths of the scintillators impose limitations on the energy resolution of the tagger hodoscope of $0.4\%E_0$ in the

horizontal part and particularly $(0.6-1.7)\%E_0$ in the vertical direction. Adjacent scintillators overlap by 55%. To mitigate background noise and enhance energy resolution, the coincidence of two neighbouring scintillators is required. As there exists a direct correlation between electron position and momentum, determining the position of the deflected bremsstrahlung electron allows for the determination of its energy E_{e^-}. Since the electrons are highly relativistic, the electron's mass can be neglected and the energy holds the relation

$$E_{e^-} = p_{e^-}$$

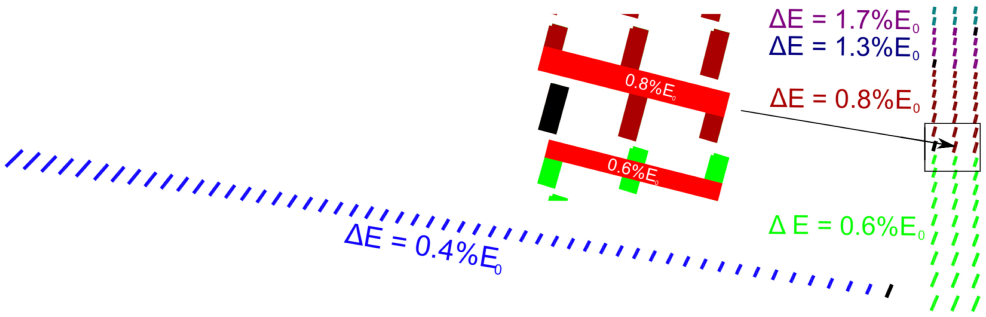

Figure 2.6: Schematic view of the tagging hodoscope, showing the plastic scintillator plates and the energy resolutions ΔE for the vertically and horizontally aligned tagging channels. In the zoomed-in region, the spatial overlap principle for coincidence channel creation is demonstrated [1]. Figure adapted from [6].

The difference

$$E_\gamma = E_0 - E_e \tag{2.1}$$

between the incoming photon beam energy and the bremsstrahlung-electron energy E_e after bremsstrahlung must equal the energy E_γ of the photon which reaches the target. After electrons leave the Tagger, they are directed towards a beam dump. Throughout this thesis, the terms *Tagger* and *tagging hodoscope* will be used interchangeably.

ARGUS scintillating fiber detector

To further improve energy resolution, a scintillating fibre detector, called *ARGUS*, is placed in front of the vertical part of the tagging hodoscope, as previously shown in Figure 2.5, complementing the BGOOD Tagger System. The use of multianode-photomultipliers instead of regular photomultiplier tubes (as used in the Tagger) allows for a more compact design [7]. Improving the energy resolution allows a finer energy binning, which is useful for many parts of the analysis at BGOOD. The energy range of an ARGUS channel depends on the physical width of the scintillation fibres, which are less wide than the scintillation plates used by the Tagger. The detector consists of 480 fibres with a diameter of 2 mm arranged in three layers and covers an energy range from 30 to 66 % of the incoming ELSA Beam energy. For a beam energy of 2.9 MeV this corresponds to an energy range of $(870-1914)$MeV. The energy resolution is between 0.1% to 0.4% of E_0 [7][8]. A detailed explanation on the reconstruction of tracks will be given in section 3.2.

2.3 Analysis Tools

Data Analysis at BGOOD is performed in the ROOT-based ExPlORA[2] Framework, which transforms the acquired data from the experimental setup into an accessible format.

2.3.1 ROOT

ROOT was developed by CERN, for handling data in particle physics. It is an extended object-oriented software, implemented in C++, which provides many useful data structures and functions to handle calculations in particle physics [9].

2.3.2 ExPlORA Framework

ExPlORA is a ROOT-based framework, which provides plugins and a basic interface to handle detector-acquired data in high-energy physics and was developed in Bonn by the CBELSA/TAPS collaboration [10]. The plugin handles physics data, acquired by the experimental readout electronics and transforms it into data, which can be used in the analysis.
Using specified detector geometry and error information, real data in each detector channel is reconstructed to obtain so-called *Hits*. Hits that were created by the same particle are then grouped into *clusters*. By combining clusters of multiple detectors that are assigned to the same particle, a *track* can be formed. All the *tracks* can then be accessed and analysed. The track reconstruction for ARGUS will be investigated in section 3.2. More about the reconstruction of tracks and the ExPlORA framework can be read in [4].

[2] Extended Pluggable Objectoriented ROOT-ified Analysis

CHAPTER 3

ARGUS efficiency analysis

The goal of the following analysis is to be able to determine cross-sections, using the ARGUS detector. Therefore the total photon flux in ARGUS binning has to be determined. Additionally the ARGUS detection efficiency will be determined, by comparing the energy spectra of the photon beam measured by the Tagger and ARGUS.

3.1 Mapping the Tagger spectrum onto the ARGUS binning

One issue that arises is that histograms must have the same binning in order to divide their contents. A bin is an interval in the x-direction that contains any number of y-values. To address this, the proportion of ARGUS bin counts that belong to each Tagger bin must be determined. Since both binnings are known this is possible by calculating the overlap region of each ARGUS channel with each corresponding Tagger channel and distributing the counts of one Tagger channel onto the ARGUS channels in front of it. For the binning of two histograms to be identical, both the number of bins and the widths of the bins must be the same. As described in subsubsection 2.2.3, the width of an ARGUS bin depends on the diameter of the scintillation fibres, and the width of a Tagger bin depends on the overlap region of the scintillation plates in the tagging hodoscope, as shown in Figure 2.6.
The following describes the partitioning of the histogram's bin contents into a finer binning. In the following analysis, the Tagger binning is mapped to the ARGUS binning.
In the simplest scenario, depicted in Figure 3.1, two ARGUS channels precisely overlap one Tagger channel.

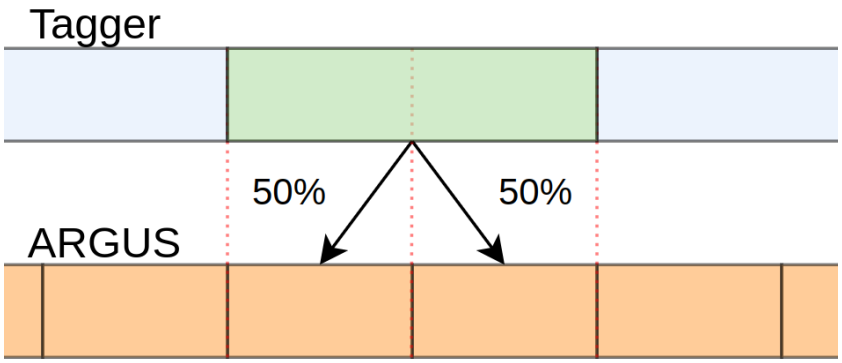

Figure 3.1: Illustration of two ARGUS channels precisely overlapping one Tagger channel.

Now, the proportion covered by an ARGUS bin over the Tagger bin can be determined. Assuming an equally distributed electron flux, 50% of the Tagger content would be assigned to each ARGUS bin[1]. Adding the events in the ARGUS bins thus results in the total number of events in the Tagger bin. This scenario applies when the number of ARGUS bins is an integer multiple of the number of Tagger bins. In practice, one Tagger channel corresponds to roughly three to five ARGUS channels. Usually, a single ARGUS bin may sometimes overlap with two Tagger channels. In such instances, it becomes necessary to calculate the portion of the ARGUS bin that corresponds to the first Tagger channel and the portion that overlaps with the second Tagger channel. This scenario can be seen in Figure 3.2.

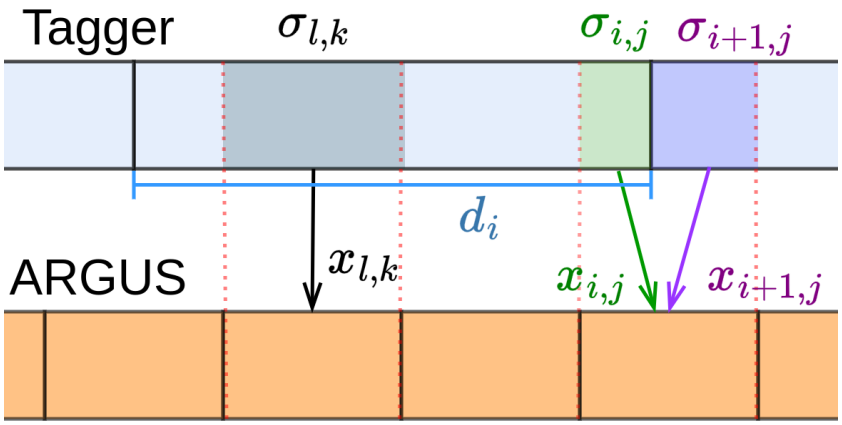

Figure 3.2: Illustration of the overlap between ARGUS and Tagger binning.

The total number of events N_j in the j-th ARGUS bin is then

$$N_j = x_{i,j} \cdot N_i + x_{i+1,j} \cdot N_{i+1} \quad , \tag{3.1}$$

where $x_{i,j}$ is the overlap-ratio of the i-th Tagger channel with the j-th ARGUS channel and N_i the number of events in the i-th Tagger channel. The ratio $x_{i,j}$ is determined from the overlap region $\sigma_{i,j}$ of

[1] Actually, the probability depends on $\frac{1}{E_\gamma}$, which will be neglected here

the i-th Tagger, the j-th ARGUS channel and the width d_i of the i-th Tagger channel;

$$x_{i,j} = \frac{\sigma_{i,j}}{d_i} \quad . \tag{3.2}$$

With these fractions, the total number of events in the Tagger channels is then distributed to the ARGUS bins.

The mapping applied to the total photon flux measured by the Tagger, is depicted in Figure 3.3. It can be observed that one Tagger bin corresponds to 3 to 4 ARGUS bins. The rebinned photon flux will later be useful for normalising the cross-section determined with ARGUS.

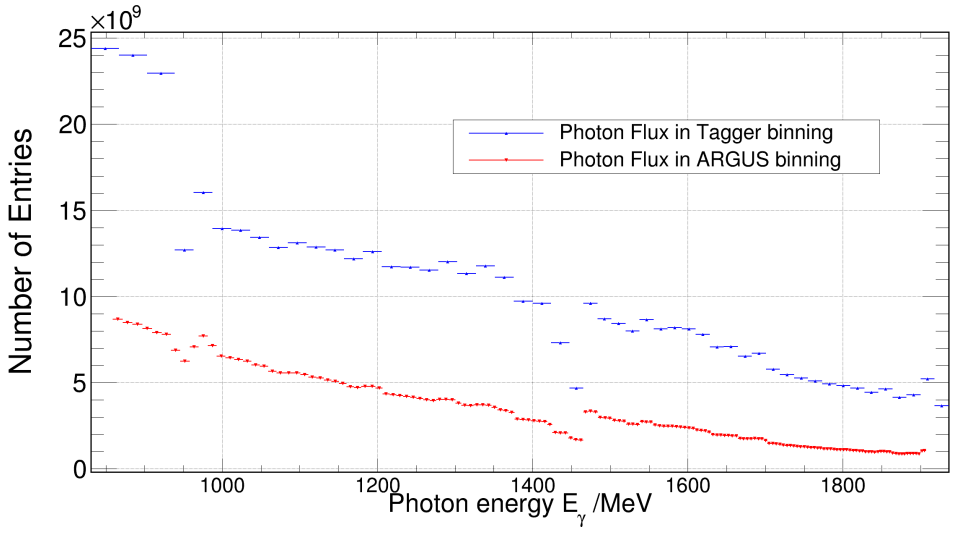

Figure 3.3: Total photon flux $N_\gamma(E_\gamma)$ in Tagger binning (blue) and ARGUS binning (red), measured by the Flumo, as described in subsubsection 2.2.3. Here only the range covered by ARGUS is shown. The total photon flux in the full range covered by the Tagger can be found in Figure A.2.

The mapping can now be applied identically to any energy spectrum measured in the Tagger-binning.

3.2 Track reconstruction with ARGUS

In subsection 2.3.2 the analysis chain at BGOOD was explained briefly. In this section, the track reconstruction of particle tracks with ARGUS will be further investigated, since it is crucial to understand how an efficiency can be obtained. The information in this section was taken from [4].
As previously shown in Figure 2.5, ARGUS is placed in front of the vertical part of the tagging hodoscope. An electron passing a scintillation fibre deposits energy in that fibre. If the signal exceeds the minimum threshold energy of 170 keV [7, p.13], the signal is registered as a hit. If neighbouring cells register a hit at a correlating time, the signals are assigned to a cluster. This can be seen in Figure 3.4. Here, the red line represents the trajectory of the electron, while the green-coloured fibres are registered as a hit. The dark blue fibres did not deposit enough energy to trigger a response. With the additional information

on the clusters seen in the Tagger, a track can be defined by combining the ARGUS cluster with the Tagger cluster. To avoid pairing accidental coincidences, selection cuts on the time difference between ARGUS and tagger of 2.5 ns is performed and the energy difference between two clusters must be less than 30 MeV [4, p.136].
Additionally, according to [4, p.135], clusters within ARGUS are limited to having between 2 and 6 hits. This limitation reduces the likelihood of cluster formation from delta electrons, as illustrated by the splitting red line in Figure 3.4, which registers as a hit in the light blue channel. It also diminishes cluster formation from noise.

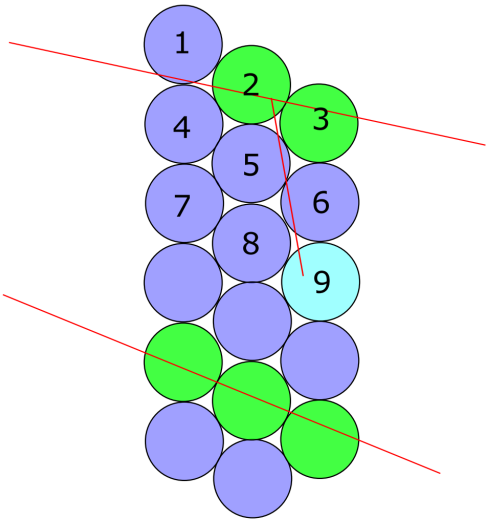

Figure 3.4: Schematic side view depicting a few ARGUS scintillation fibres. Trajectories of electrons are highlighted in red. Blue fibres indicate insufficient energy deposition, while green fibres correspond to clustered events. Adapted from [7, p. 14].

3.3 Determination of the relative ARGUS detection efficiency

It is possible to assess the relative efficiency of ARGUS by calculating the ratio of events detected by ARGUS to those observed by the tagging hodoscope across the covered energy spectrum. The equation for the efficiency is given in (3.3).

$$\text{relative ARGUS detection efficiency} = \frac{\text{events measured by ARGUS}}{\text{events measured by the Tagger}} \tag{3.3}$$

The full individual spectra of photon energies E_γ, acquired by the measurements on the post-bremsstrahlung electrons performed with ARGUS and the Tagger, explained in subsection 2.2.3, are depicted in Figure A.1. In Figure 3.5, the energies measured by ARGUS and the Tagger are presented in the energy region covered by ARGUS.

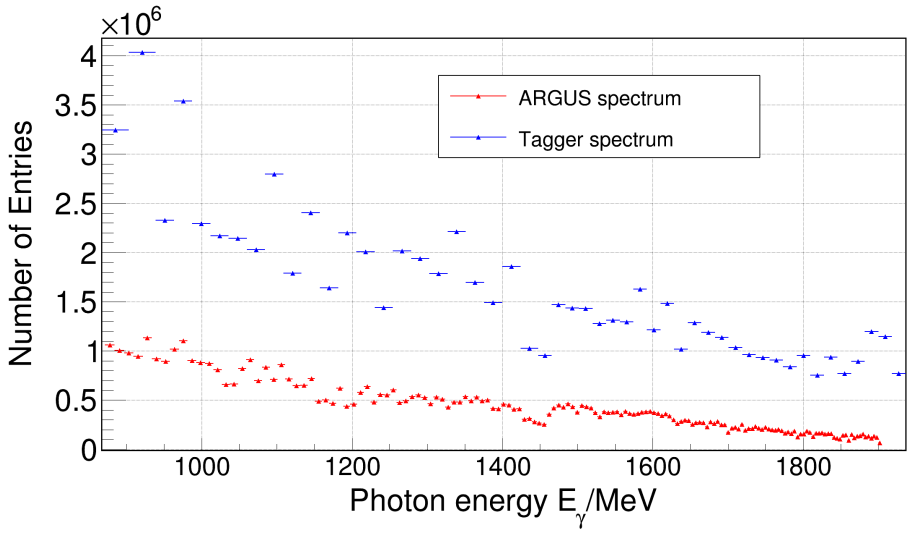

Figure 3.5: Post bremsstrahlung photon energy spectrum measured by ARGUS and Tagger in the energy range covered by ARGUS from 870 MeV to 1 914 MeV.

Note, that the ARGUS binning and Tagger binning are not identical, as the ARGUS scintillating fibres are much finer. This can be observed in the plot, where individual ARGUS bins are smaller than those of the Tagger bins and contain fewer entries. The challenge here is that the ARGUS bins do not precisely align with a Tagger bin; instead, an ARGUS bin sometimes overlaps with two Tagger bins. However, the mapping method, explained in section 3.1 fixes this problem and the Tagger spectrum in ARGUS bins is obtained. Both spectra in ARGUS binning can be seen in Figure 3.6.

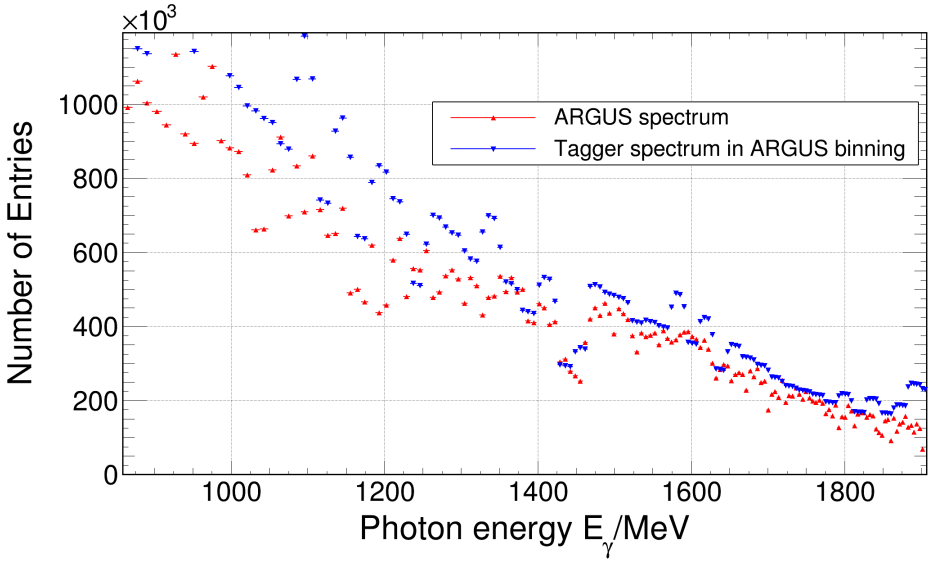

Figure 3.6: Spectra measured by the Tagger and ARGUS, organized in ARGUS binning. The Tagger spectrum in ARGUS bins was derived using the mapping method from section 3.1.

Since the spectra are now in the same binning, the contents of their bins can be divided by each other, following (3.3). The resulting relative ARGUS efficiency, depending on the photon energy E_γ , is shown in Figure 3.7.

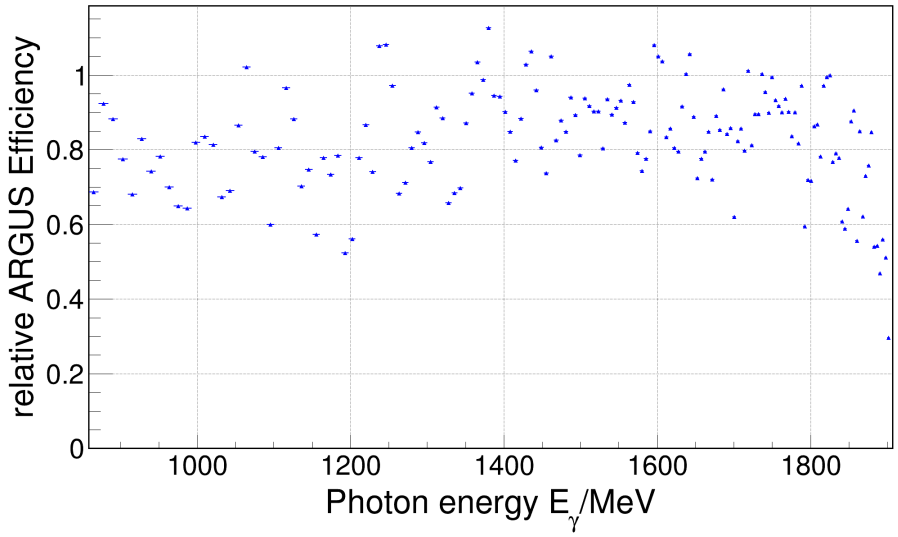

Figure 3.7: ARGUS detection efficiency relative to the detection efficiency of the Tagger.

It reaches values between 0.6 up to slightly above 1. In principle values larger than 1 should not be possible, since the Tagger seeing an electron is a requirement for ARGUS to measure a particle passing. This will be further discussed in the next section.

3.4 Inefficiencies and systematic errors

It is shown, that ARGUS has an average detection efficiency of around 80%, relative to the Tagger. Naturally, the question arises as to why this value is not at 100%. This can be explained by the fact that electrons must deposit a minimum energy of 170 keV [7, p.13] in the scintillating fibres for the channel to trigger. The energy deposited by an electron in a scintillating fibre depends on the distance from the centre of the fibre. Therefore, it is possible that electrons grazing a scintillating fibre may not be registered as a hit.

Contrary to expectations, it can be observed in Figure 3.7 that the relative efficiency is greater than 1 for some energies. This contradicts the expectancy that ARGUS should only detect an event if the Tagger detects an electron. However, there are other factors that could potentially result in an apparent efficiency greater than one for ARGUS, as explained in the next section.

3.4.1 δ-electrons

As explained in section 3.2, δ-electrons are generated within the fibres and can potentially build clusters within ARGUS. However, given that this is a statistical process that could manifest in all ARGUS channels, it is unlikely to be the root cause for single bins having an efficiency >1.

3.4.2 Incorrect assignments of ARGUS bins to Tagger bins

The number of ARGUS clusters per Tagger cluster, also known as multiplicity, is now plotted against the Tagger energy, as shown in Figure Figure 3.8. For this to be an explanation for the relative ARGUS efficiency being larger than one, the number of ARGUS clusters per Tagger cluster should be larger than one by a significant amount at affected energy bins.

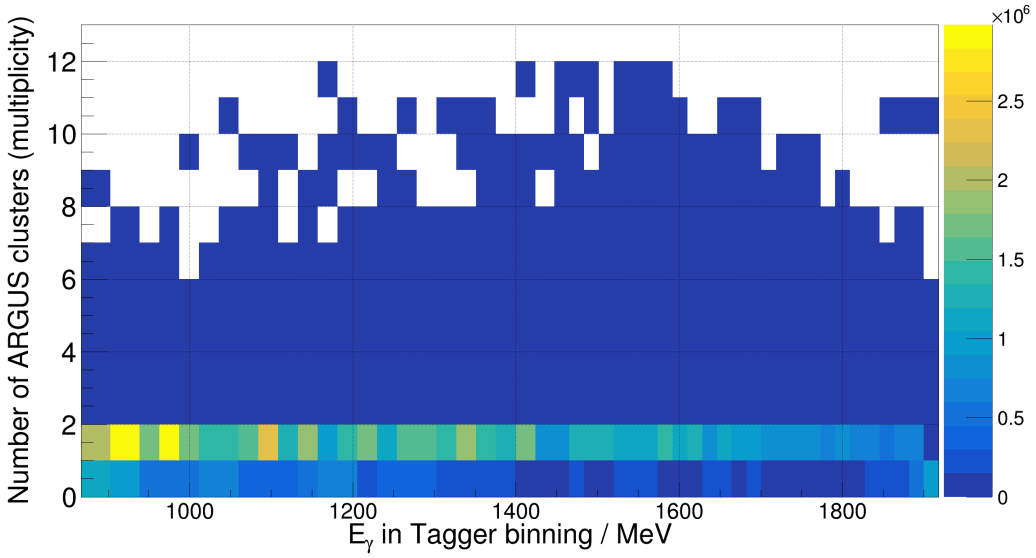

Figure 3.8: Multiplicity as a function of E_γ measured by the Tagger.

As can be seen, in most cases, 0 or 1 ARGUS clusters are assigned to a Tagger cluster. In a tiny amount of cases, more than one ARGUS cluster is measured for one Tagger hit. This is caused, as previously explained, by δ-electrons and low energy background from the accelerator. The Y-projection of a single bin from Figure 3.8 is depicted in Figure 3.9, which illustrates the number of events against the multiplicity for one ARGUS bin in an energy range from $(1254 - 1279)$MeV. It shows that essentially 0 or 1 ARGUS-cluster is found for each Tagger-cluster. The projection looks similar for all energy bins in the energy range covered by ARGUS and shows clearly, that the number of events with more than one ARGUS cluster is negligible.

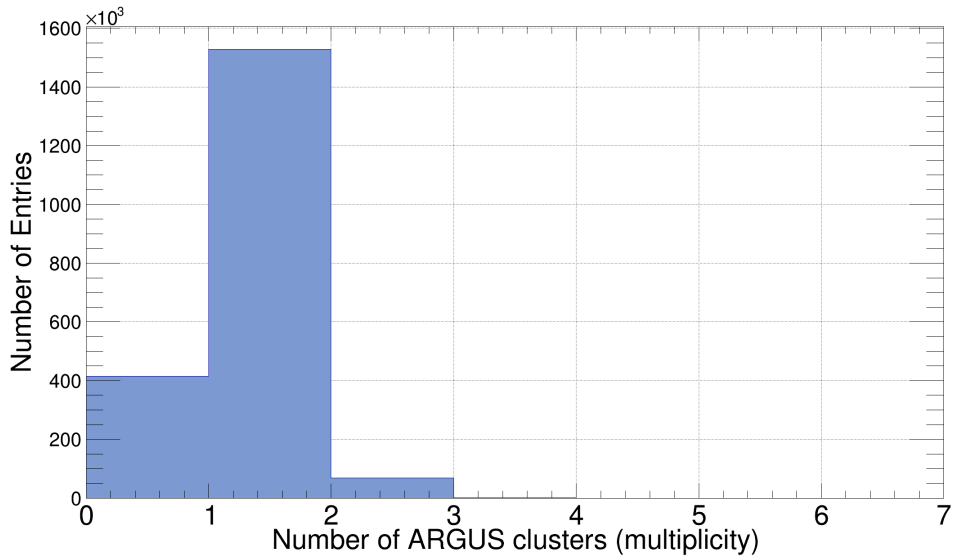

Figure 3.9: Number of entries in the spectrum measured by ARGUS against multiplicity in the energy range of (1254 – 1279)MeV (one bin).

Therefore, it is unlikely that ARGUS, detecting more events than it should in individual energy bins, is the cause for an efficiency > 1.
To check if the Tagger energies are assigned to the ARGUS energies properly, the energy bins are plotted against each other in a 2D histogram, seen in Figure 3.10.

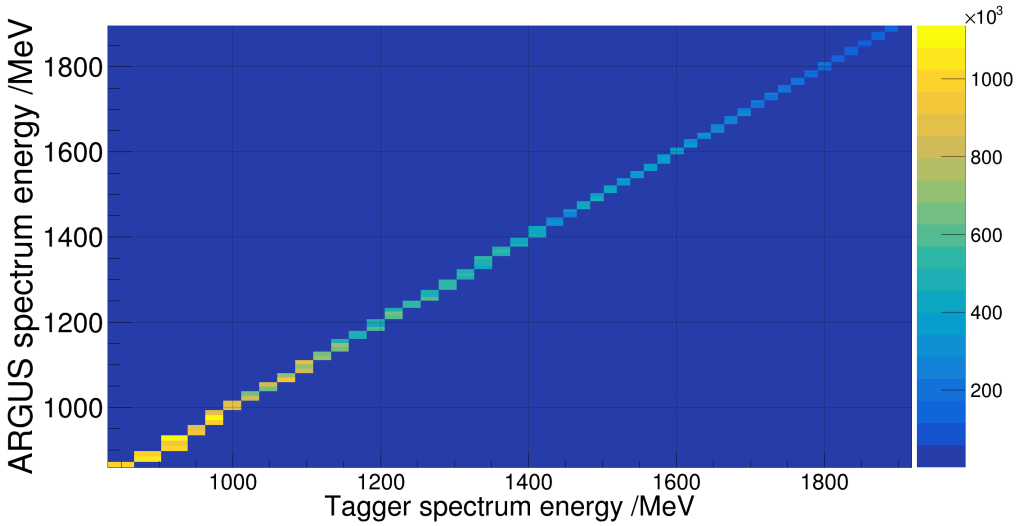

Figure 3.10: Energy spectra measured by ARGUS and the Tagger in a 2D-Plot to look for false assignments of ARGUS to Tagger energies.

A strong correlation between the Tagger and ARGUS is visible, so no obvious incorrect assignments are apparent here.

3.4.3 Noisy ARGUS channels

Another source of error could technically be a noisy ARGUS channel. This would be a channel with e.g. broken electronics that triggers events, even tho no hits should be registered. By looking at Figure 3.9 and Figure 3.10 this can be excluded since this would result in an increase in multiplicity and in a severely increased number of entries at a certain ARGUS energy.

3.4.4 Inaccuracies in ARGUS bin widths

Another cause may be due to inaccuracies in determining the energy borders of ARGUS by a few MeV. Since the very thin fibres and the requirement for high precision both in the physical arrangement and installation of the detector, as well as in the determination of energy widths, this is by no means unlikely. The deviation in efficiency is small enough that it can still be used for measurements with ARGUS, however, the limitations and possible inefficiencies have to be kept in mind.

3.5 Stability Studies

Several properties of reaction channels, such as the cross-section, are highly dependent on detection efficiency. It is therefore essential to exclude whether the determined relative efficiency of ARGUS changes, over time during the data acquisition process, or under different photon rates. To address this, two different beam times will be analysed. Initially, the variation in efficiency will be plotted at the start of a beam time, after one week, and after two weeks. Ideally, the efficiency of each channel should remain consistent throughout. In the following section, three runs with different photon rates will be compared.

3.5.1 Time dependency

In the following, the data from the 2018 beam time will be analysed. Plotting the relative ARGUS efficiency of three different days, depicted in Figure 3.11, shows only small deviations in the efficiency and in most cases the errorbars overlap.

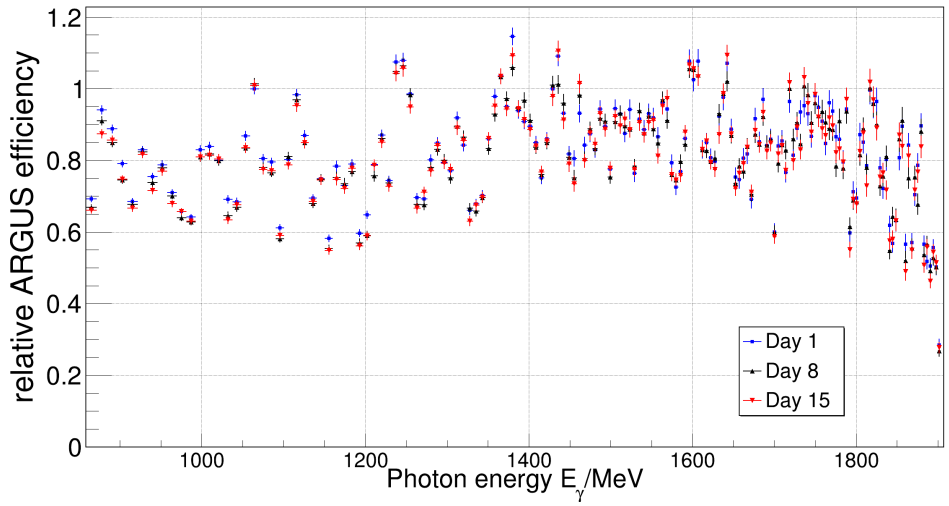

Figure 3.11: Efficiencies of three runs after different times. First Day (blue), 8th Day(black), 15th Day (red)

To check for a trend, the initial efficiency at the beginning of the beamtime will be divided by the efficiency after 8 days and by the efficiency at the end of the beamtime. The obtained trend is shown in Figure 3.12.

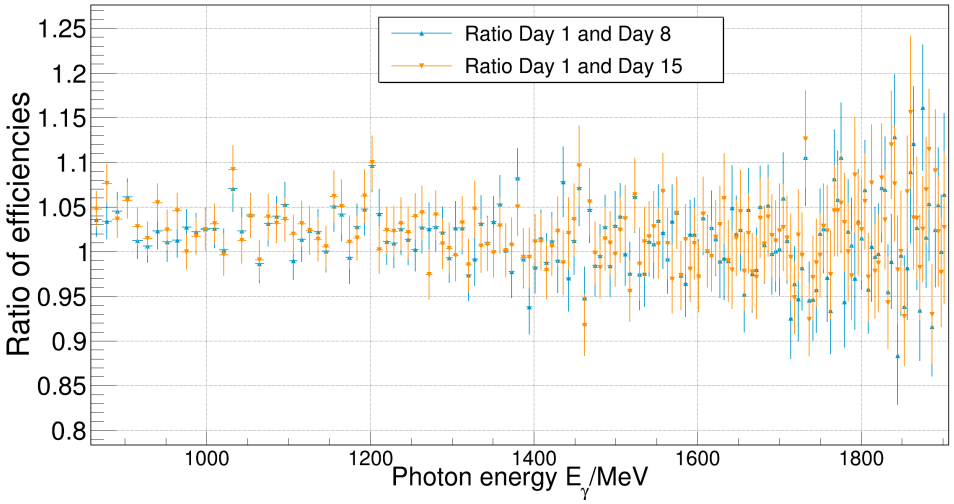

Figure 3.12: Ratio of the initial efficiency after the 8th day (blue) and the ratio of the initial efficiency after the 15th day (orange).

It shows that even tho the efficiencies deviate slightly in the lower energy region, almost all errorbars overlap and agree with a value of 1. Thus, the efficiency does not significantly change over time and the small deviations are due to statistical fluctuations.

3.5.2 Photon rate dependency

To check if the relative ARGUS efficiency depends on the photon rate, the efficiency is determined for two runs with different rates, depicted in Figure 3.13.

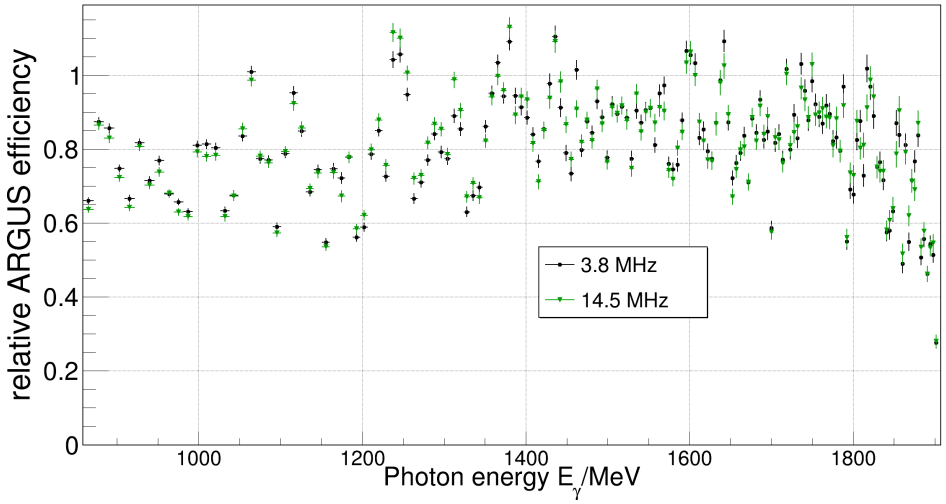

Figure 3.13: Efficiencies of two runs with different tagging rates. 14.5 MHz (green) and 3.8 MHz(black)

As a measure for the photon rate, the rate measured by the Tagger is used. It can again be observed, that the efficiency is within the statistical limits. Analogous to subsection 3.5.1, a ratio of the efficiencies is used to investigate if there is a trend, shown in Figure 3.14.

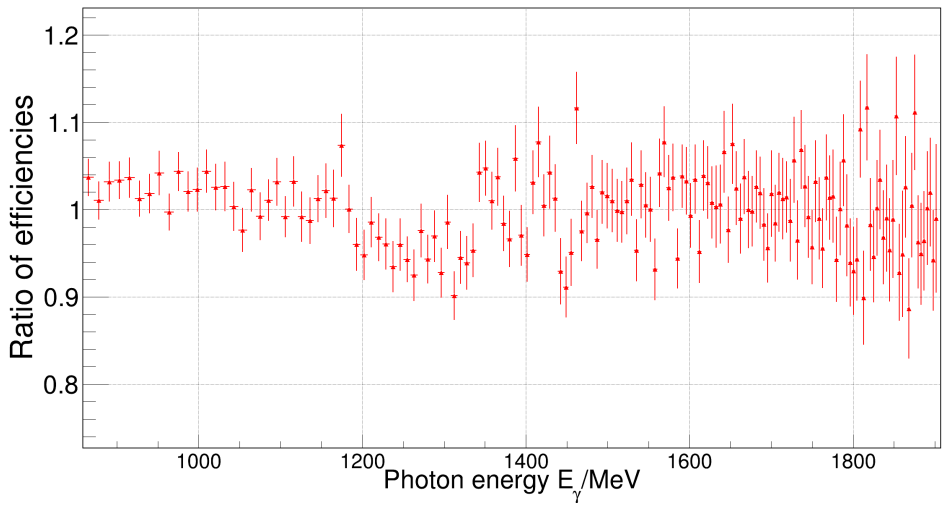

Figure 3.14: Efficiency at low photon rate of 3.8 MHz divided by the efficiency at a higher photon rate of 14.5 MHz, shown in Figure 3.13

Looking at the values and errorbars, it can be seen that the ratio of efficiencies is approximately one at all energies, which shows that there is no trend to be seen. However, there are some bins where the efficiency seems to increase with photon rate, especially in the energy region from 1 190 MeV to 1 330 MeV.

CHAPTER 4

Determining the $\gamma p \rightarrow \eta p$ differential cross section

In the following chapter, the result for the relative ARGUS detection efficiency will be put to test, by an attempt to determine the η-photoproduction cross section, using the ARGUS detector. To verify and compare the results with the Tagger, the analysis steps to obtain the cross-section will be shown for both detectors.
The differential cross-section derives from the following equation:

$$\frac{d\sigma(\theta, E_\gamma)}{d\Omega} = \frac{N(\theta, E_\gamma)}{N_{\text{Flux}}(E_\gamma) \cdot \rho \cdot \Omega \cdot l \cdot \epsilon(\theta, E_\gamma)}, \tag{4.1}$$

where $N(\theta, E_\gamma)$ is the number of reaction particles measured by a detector after applying selection cuts, $N_{\text{Flux}}(E_\gamma)$ is the total photon flux, depicted in Figure A.2, ρ is the target density and l the length of the used target, Ω is the solid angle in which the cross-section is determined and $\epsilon(\theta, E_\gamma)$ is the reconstruction efficiency for the observed reaction.
The density of the used liquid hydrogen target is [5, p.36]

$$\rho = 4.237 \cdot 10^{-8} \frac{1}{\mu\text{b} \cdot \text{cm}}, \tag{4.2}$$

which has to be multiplied by the length of $l = 11$ cm of the target to get the area density.

This chapter will be divided into three sections. In the first, an overview of the observed reaction will be provided, briefly explaining the physics and phenomena of the η-photoproduction. After this, the techniques on how to extract the desired reaction channel from the data will be explained. Finally, the cross-section will be determined and discussed. Since the total photon flux is already known, only the reconstruction efficiencies $\epsilon(\theta, E_\gamma)$ and the number of reaction particles $N(\theta, E_\gamma)$, detected with either the Tagger or ARGUS have to be determined.

4.1 Physics of the η-photoproduction

In η-photoproduction off the proton, a photon hits a proton inside the hydrogen target. As a result either an intermediate state of mesons or the final state, consisting of an η and a proton, is produced. The η particle decays quickly through one of the decay modes, listed in Figure 4.1. The highest branching ratio Γ_i/Γ, which represents the likelihood of a decay, has the decay into two photons [11].

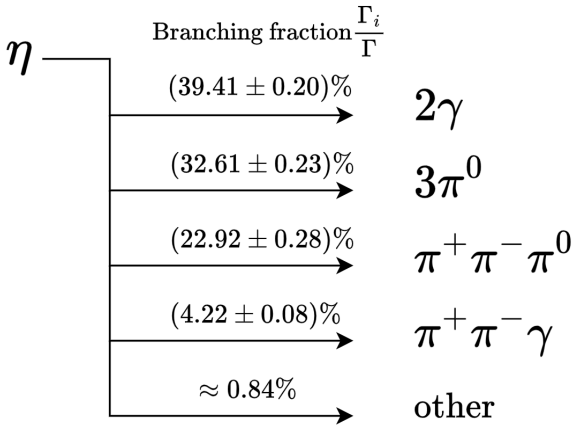

Figure 4.1: Eta decay scheme. Data from [11].

The threshold energy in the lab frame for η-photoproduction derives from energy conservation and is calculated in (4.3)

$$E_{\text{lab}}^{\text{thr}} = \frac{m_\eta^2 + 2m_\eta m_p}{2m_p} \approx 708\,\text{MeV}, \tag{4.3}$$

where $m_\eta = 548\,\text{MeV}$ is the mass of the η-particle and $m_p = 938\,\text{MeV}$ is the proton mass [12]. More about the η-photoproduction of the proton can be read in [13].

4.2 Identification of particles and selection cuts

As shown, the highest branching ratio for the η has the decay into two photons. Since the BGO is stands out at detecting photons, it makes sense to reconstruct this particular reaction. Therefore the data can be reduced to events that have exactly two photons in the BGO. Additionally, since the final state includes a proton, it makes sense to only acquire events that have a proton in the forward spectrometer. Also, the number of charged particles in the BGO has to be zero. Since the η-photoproduction threshold $E_{\text{lab}}^{\text{thr}}$ is around 708 MeV the events taken into account start at a minimum beam energy of $E_\gamma = 600\,\text{MeV}$. The two photons which are detected in the BGO are combined. If the invariant mass of the 2γ system is consistent with the nominal η mass, it is classified as an η-candidate. The applied cuts on the invariant mass of the 2γ system are shown in Figure 4.2.

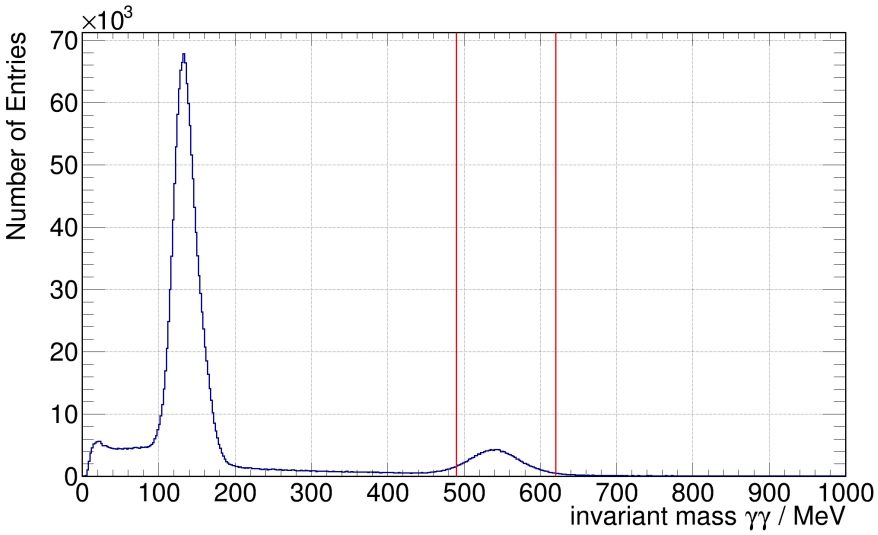

Figure 4.2: Invariant mass of two photons systenms in the BGO. The left peak is the decay of produced pions, with an energy of 135 MeV into two photons [14]. The area between the two red lines $(490 - 610)$MeV are the entries which correspond to an η.

Additionally the mass of the charged particle detected in the forward spectrometer has to be consistent with the proton mass. The applied cuts on the reconstructed mass in the forward spectrometer are illustrated in Figure 4.3

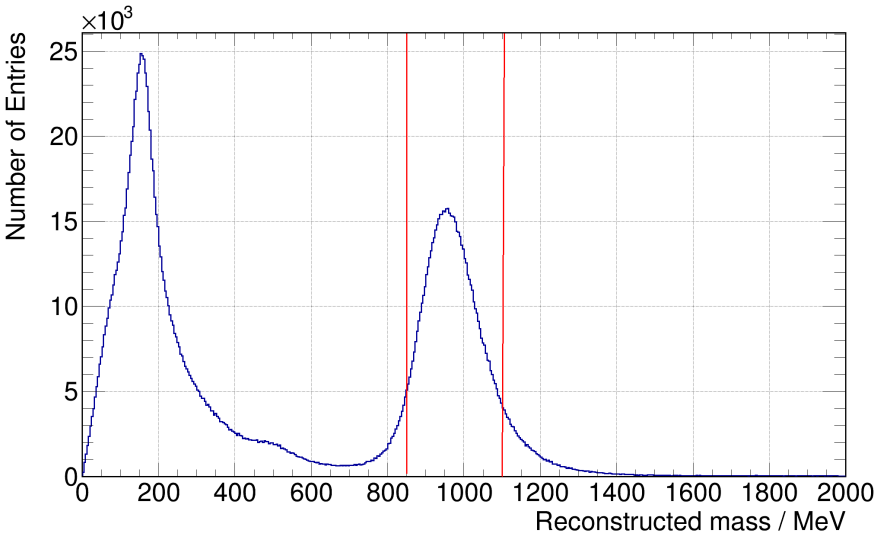

Figure 4.3: Reconstructed mass of the particles in the forward spectrometer. The area between the two red lines $(850 - 1100)$MeV are the entries which correspond to a proton. The peak on the left is caused by charged pions in the forward spectrometer with an energy of 140 MeV [14].

Since the target proton is at rest, the 4-vector of the γp initial state can be constructed from the beam

energy of 2.9 GeV and proton mass m_{proton}. The 4-vector of the ηp final state is reconstructed with the data from the forward spectrometer and the BGO. The invariant mass of the missing four-momentum between these states is called total missing mass

$$m_{\text{tot,missing}} = (p_{\text{in}} - p_{\text{fin}})^2 \tag{4.4}$$

and should be around zero. Therefore, cuts are applied as shown in Figure 4.4.

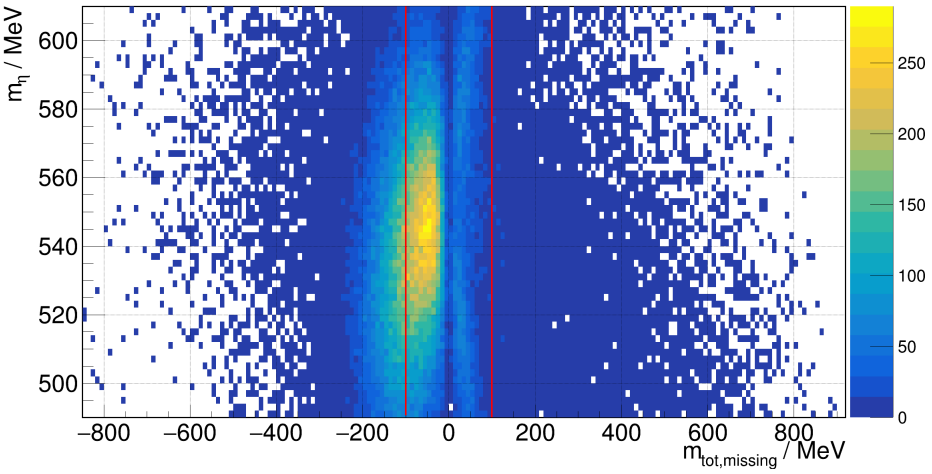

Figure 4.4: η mass vs. total missing mass in MeV. The red lines represent the cuts performed on the data. Only states with a total missing mass of $|m_{\text{tot,missing}}| < 100$ MeV are considered in the analysis.

Since the η and proton should decay at an angle of 180° in the center of mass System, cuts on the polar and azimuthal scattering angles are applied, which are shown in Figure 4.5 and Figure 4.6.

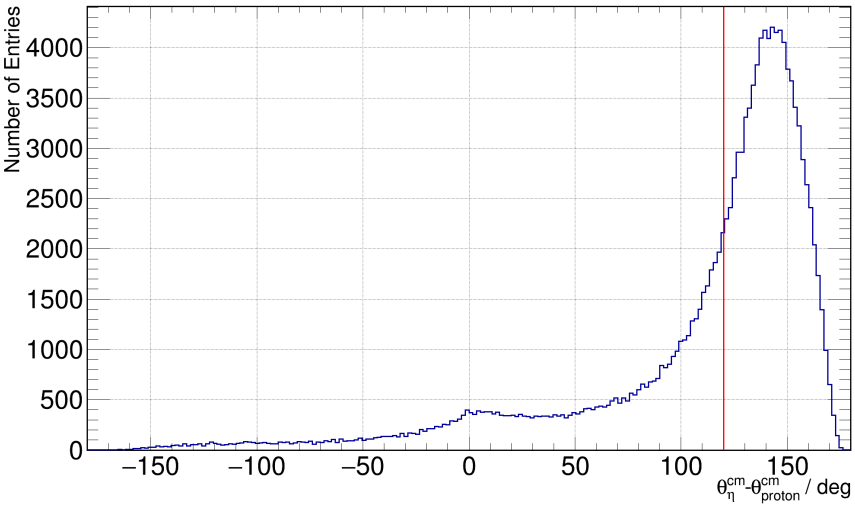

Figure 4.5: Cuts performed on the polar angle between the η and proton in the center of mass (COM) system. Only entries with $\theta_\eta^{\text{cm}} - \theta_{\text{proton}}^{\text{cm}} > 120°$ are considered in the analysis.

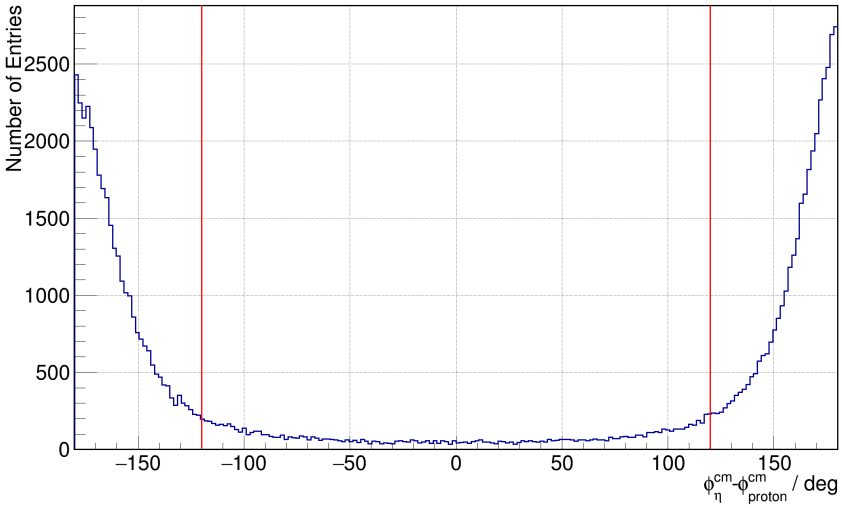

Figure 4.6: Cuts performed on the azimuthal angle between the η and proton in the center of mass (COM) system. Only entries with $|\phi_\eta^{\text{cm}} - \phi_{\text{proton}}^{\text{cm}}| > 120°$ are considered in the analysis.

Additionally only events with the proton in very forward angles and very backwards angles of the η are considered in the analysis. The cuts are shown in Figure 4.7 and Figure 4.8.

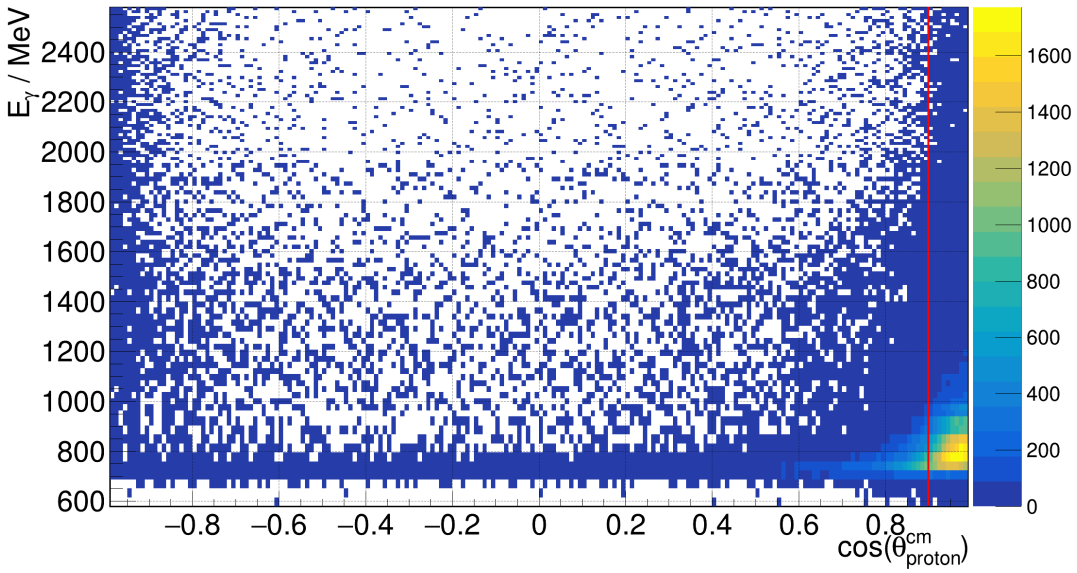

Figure 4.7: Selection cut on very forward angles of the proton. Only events with $\cos\theta^{\mathrm{cm}}_{\mathrm{proton}} > 0.9$ are considered in the analysis.

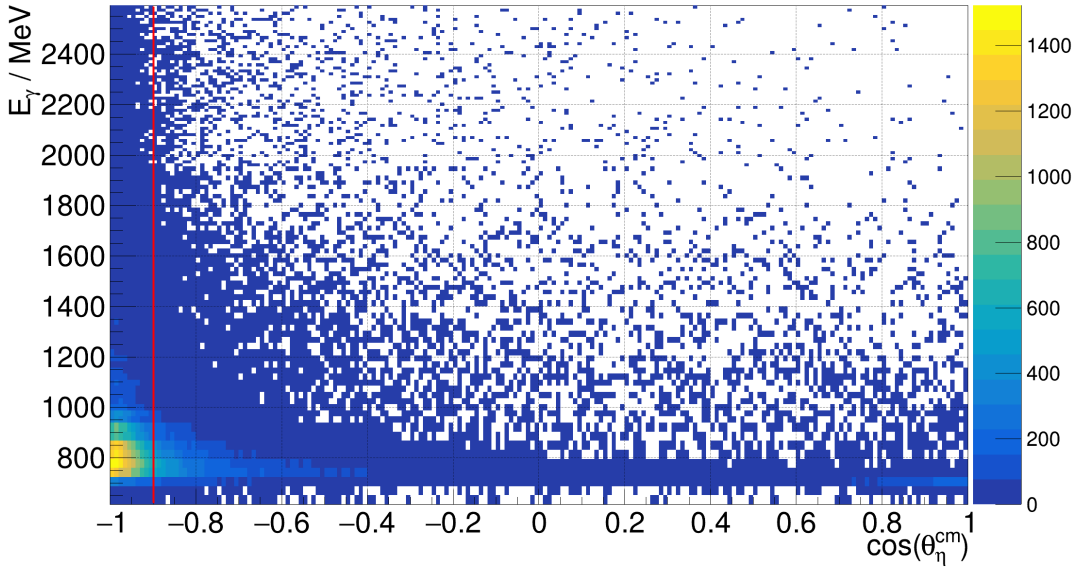

Figure 4.8: Selection cut on very backward scattering angle of the η. Only events with $\cos\theta^{\mathrm{cm}}_{\eta} < -0.9$ are considered in the analysis.

An overview of all applied cuts can also be found in Table 4.1.
Since only very forward angles are considered, the solid angle for very forward protons with $\cos\theta^{\mathrm{cm}}_{\mathrm{Proton}}$,

needed for the cross-section determination from (4.1), is calculated in (4.5).

$$\Omega = \int_0^{2\pi} \int_{\theta_1}^{\theta_2} \sin\theta d\theta d\phi = 2\pi \int_{\cos\theta_1}^{\cos\theta_2} d(\cos\theta) = 2\pi \int_{0.9}^{1} d(\cos\theta) = 2\pi(1 - 0.9) = 0.2\pi \tag{4.5}$$

.

Property	**Cut**
invariant mass $\gamma\gamma$	$(490 - 610)$MeV
reconstructed mass FS proton	$(850 - 1100)$MeV
$\lvert m_{\text{tot,missing}} \rvert$	< 100 MeV
$\theta^{\text{cm}}_{\text{Proton,Eta}}$	> 120 deg
$\lvert \phi_{\text{Proton,Eta}} \rvert$	> 120 deg
$\cos\theta^{\text{cm}}_{\text{Proton}}$	> 0.9
$\cos\theta^{\text{cm}}_{\eta}$	< -0.9

Table 4.1: Selection cuts performed to obtain the desired initial and final states

Note that the final cross-section should not depend on the statistical precision of the selection cuts and that they can be chosen by hand. After applying these cuts, the number of reaction particles measured by the Tagger and ARGUS are depicted in Figure 4.9 and Figure 4.10, as a function of the photon energy E_γ.

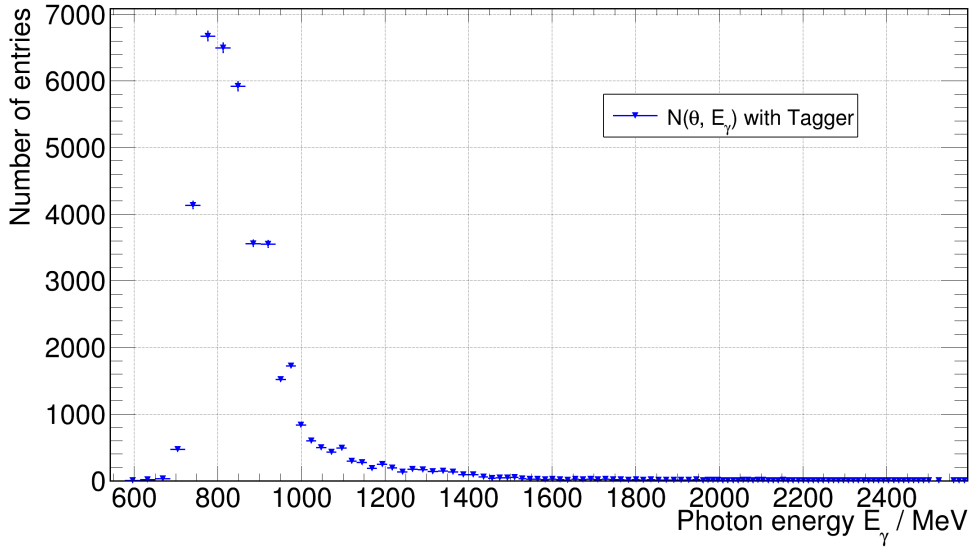

Figure 4.9: Number of reaction particles $N(\theta, E_\gamma)$ with the Tagger.

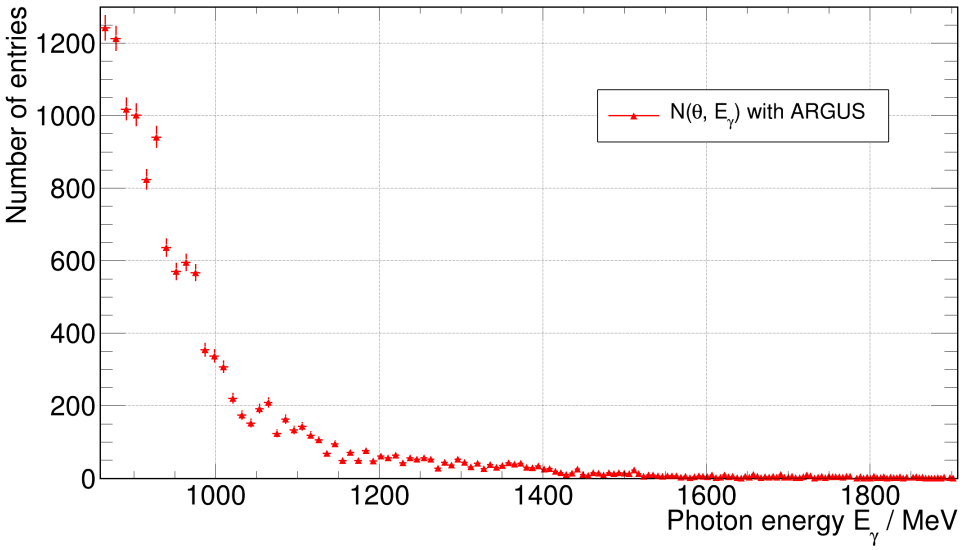

Figure 4.10: Number of reaction particles $N(\theta, E_\gamma)$ with ARGUS.

Since ARGUS only covers an energy range from $(870 - 1\,914)$MeV[1] the large peak around 800 MeV that one can see with the Tagger, is not captured by ARGUS. However, the descent of the peak can be seen. Now that the number of reaction particles has been determined, only the reconstruction efficiency $\epsilon(\theta, E_\gamma)$ is needed for a cross-section determination.

4.3 Reconstruction efficiency

The reconstruction efficiency $\epsilon(\theta, E_\gamma)$ is the probability of a produced final state to make it through the selection cuts, which are applied in the analysis. Since in a real experiment the amount of initial particles is not known, for the reconstruction efficiency data from a Monte-Carlo simulation is used, which simulates the physics of the reaction and geometry of the BGOOD-detector using Geant4[2][15]. In this case, the number of generated particles which go into the physics model is known. The reconstruction efficiency $\epsilon(\theta, E_\gamma)$ is the fraction of generated initial particles and measured particles

$$\epsilon(\theta, E_\gamma) = \frac{\text{measured particles}}{\text{generated particles}}. \tag{4.6}$$

Analogue to section 4.2 the analysis is performed with the simulated data and the number of reconstructed particles is divided by the number of generated particles to obtain the reconstruction efficiency.
Since the ARGUS detector efficiency is unknown to the physics model, and therefore assumed to be 100%, the reconstruction efficiency for ARGUS and Tagger from the simulation are the same value, but with a different binning, as depicted in Figure 4.11.

[1] which corresponds to $(0.3 - 0.66)\%$ of incoming beam energy of 2.9 GeV as discussed in section 2.2.3.
[2] Geometry and Tracking 4

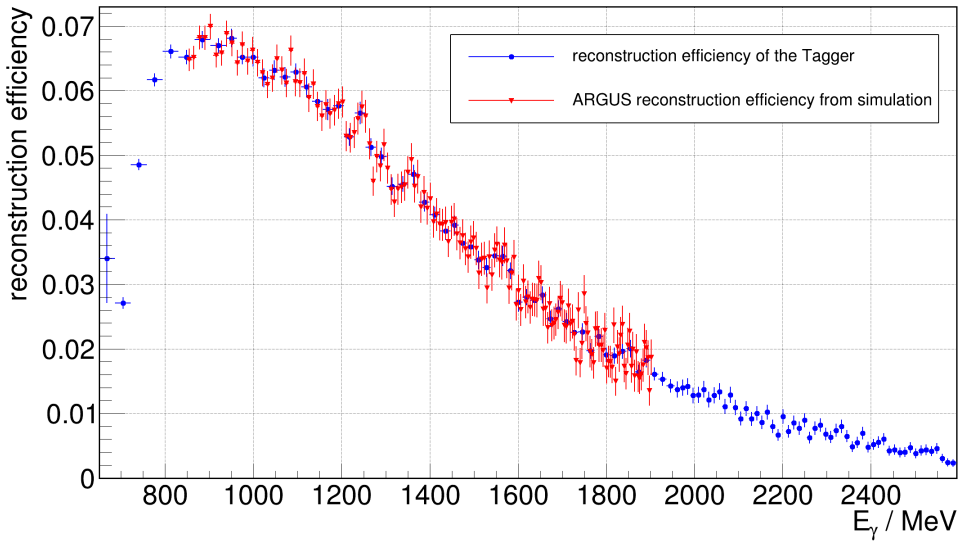

Figure 4.11: Reconstruction efficiency $\epsilon(\theta, E_\gamma)$ from the simulation of ARGUS and the Tagger. As explained in the text the ARGUS one will be corrected by the in chapter 3 determined relative ARGUS detection efficiency. The resulting true ARGUS reconstruction efficiency will be shown in Figure 4.12.

To acquire the *true* ARGUS reconstruction efficiency, ARGUS reconstruction efficiency from Figure 4.11 is multiplied binwise with the relative ARGUS detection efficiency, previously depicted in Figure 3.7. The resulting true reconstruction efficiency for ARGUS is shown in Figure 4.12.

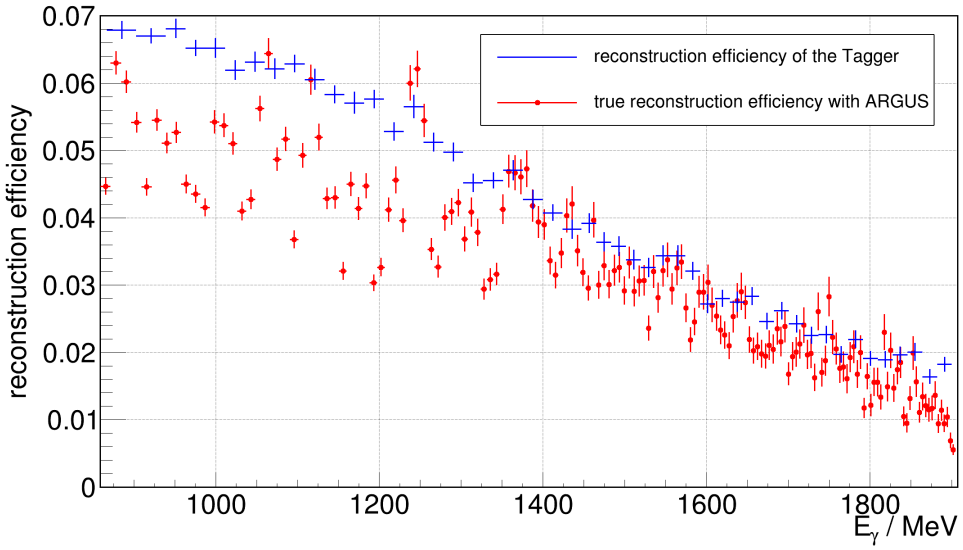

Figure 4.12: True reconstruction efficiency with ARGUS in comparison to the reconstruction efficiency from the Tagger.

As expected, the obtained reconstruction efficiency with the ARGUS detector is therefore a little lower than with the Tagger.
Now that all the ingredients have been found, the cross-section for the η-photoproduction can be determined.

4.4 Differential cross section calculation

The differential cross-section is determined as described in (4.1), using either the Tagger or ARGUS for reconstruction. The flux normalisation of the cross-section determined with the Tagger, is performed with the total photon flux in the original Tagger binning, shown in Figure A.2. For the normalisation of the cross-section determined using ARGUS, the total photon flux mapped onto the ARGUS binning, which is depicted in Figure 3.3 is used[3]. The resulting cross-section, in the overlap region of Tagger and ARGUS in an angular bin of $\cos\theta_{\eta}^{\mathrm{cm}} < -0.9$, together with the parametrisation from Bonn Gatchina [16], is shown in Figure 4.13.

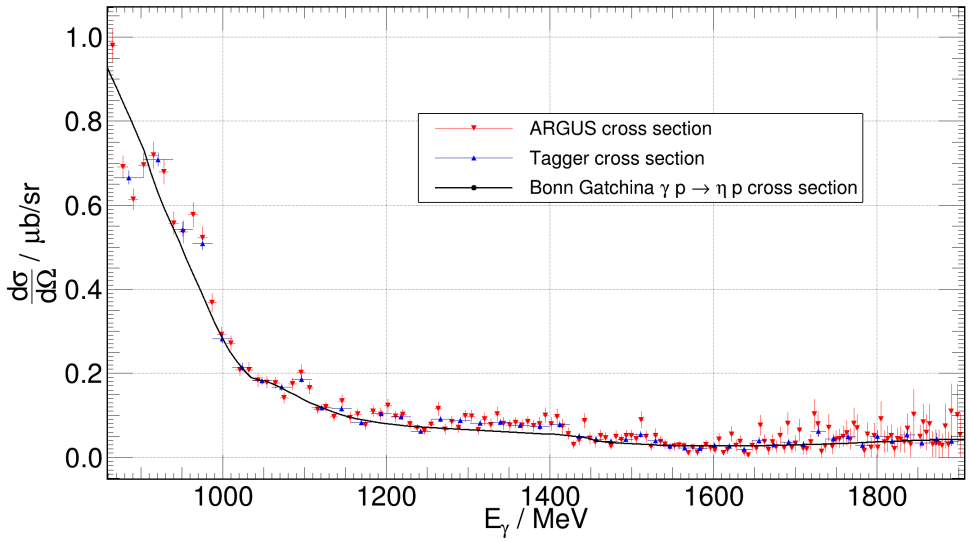

Figure 4.13: Differential cross section for $\cos\theta_{\mathrm{Proton}}^{\mathrm{cm}} > 0.9$ as a function of the photon beam energy E_{γ}. The black line represents the parametrisation from the Bonn Gatchina Partial Wave Analysis [16].

Both results agree with each other and the theoretical model, which shows, that the determination of the relative ARGUS efficiency is correct and the applied tools and methods work well.

[3] The method behind the mapping was explained in detail in section 3.1

CHAPTER 5

Conclusion

The aim of the analysis was to find a way to determine the $\gamma p \rightarrow \eta p$ cross-section, using the ARGUS detector. A key step was to rebin the total photon flux from the Tagger binning into the ARGUS binning and the determination of the ARGUS detection efficiency relative to the Tagger.
The $\gamma p \rightarrow \eta p$ cross-section was successfully determined, what shows that the applied methods work well.
However, to be able to ensure that the data taken is 100% correct, the ARGUS binning has to be investigated in the future, since it was found that the ARGUS efficiency relative to the Tagger was in some cases larger than one. The most likely cause are small shifts of the bin borders. Since even a small deviation of a few percent in the determined detection efficiency can have significant effects on further calculations in the analysis, this has to be kept in mind.
The next step could be to apply the method for other reaction channels and include the relative ARGUS detection efficiency determination in the simulation.

APPENDIX A

Additional Information

In the following, the individual post-bremsstrahlung photon spectra measured by both the Tagger and ARGUS are displayed. In chapter 3 of the analysis, only the region covered by ARGUS is depicted.

A.1 Spectra measured by ARGUS and tagging hodoscope

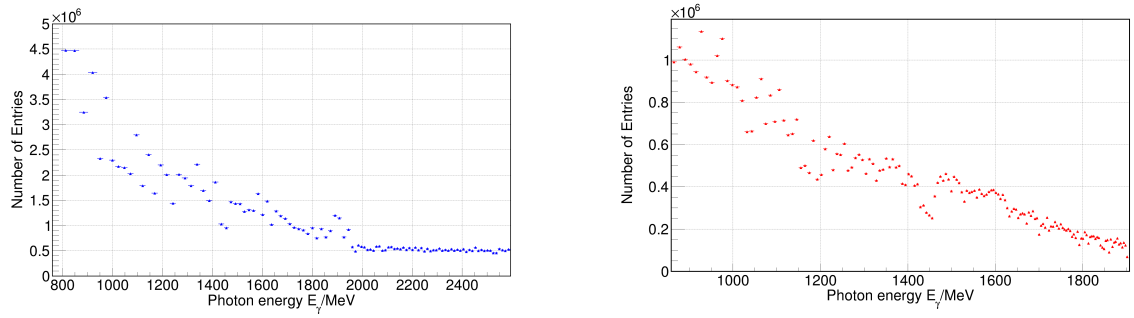

(a) Full spectrum measured by the Tagger

(b) Full spectrum measured by ARGUS

Figure A.1: Full individual post-bremsstrahlungs photon spectra measured with the Tagger and ARGUS, as described in subsection 2.2.3. Used in Figure 3.5.

Furthermore the total photon flux in the Tagger binning is shown in Figure A.2. In section 3.1 of the analysis only the region covered by ARGUS was illustrated.

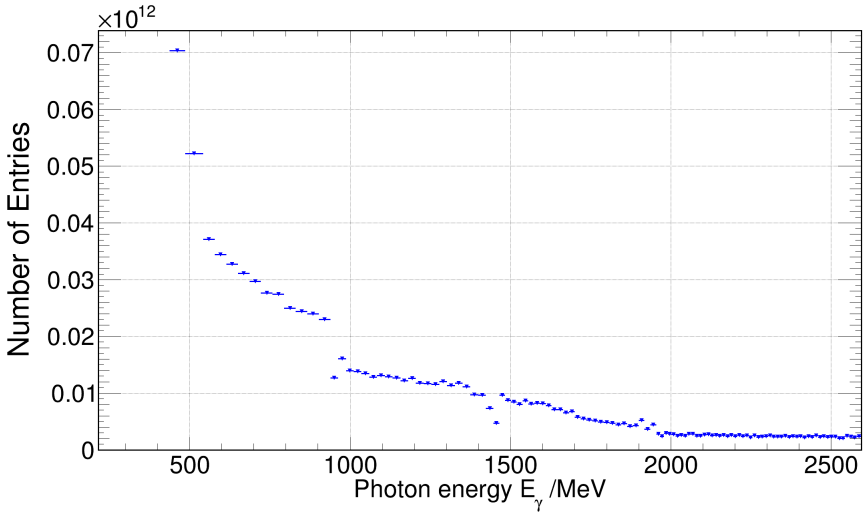

Figure A.2: Total photon flux in the Tagger binning used in Figure 3.3.

Bibliography

[1] Alef, S. et al., *The BGOOD experimental setup at ELSA*, Eur. Phys. J. A **56** (2020) 104, URL: https://doi.org/10.1140/epja/s10050-020-00107-x (cit. on pp. 1–3, 6, 7).

[2] *ELSA*, URL: https://www-elsa.physik.uni-bonn.de/index_en.html (visited on 30/03/2023) (cit. on p. 2).

[3] W. Hillert et al., *Beam and spin dynamics in the fast ramping storage ring ELSA: Concepts and measures to increase beam energy, current and polarization*, EPJ Web Conf. **134** (2017) 05002, ed. by F. Klein, U. Meißner and U. Thoma (cit. on p. 3).

[4] Oliver Freyermuth, *Studies of ω Photoproduction off Proton at the BGO-OD Experiment*, PhD thesis: Rheinische Friedrich-Wilhelms-Universität Bonn, 2017, URL: https://hdl.handle.net/20.500.11811/7263 (cit. on pp. 4, 8, 11, 12).

[5] G. Scheluchin et al., *Photoproduction of $\Lambda(1405)$ extending to forward angles and low momentum transfer*, Physics Letters B **833** (2022) 137375, ISSN: 0370-2693, URL: https://www.sciencedirect.com/science/article/pii/S0370269322005093 (cit. on pp. 5, 6, 21).

[6] A. Bella, *Linearly polarised photon beams at the BGO-OD experiment at ELSA*, (2016), URL: https://hss.ulb.uni-bonn.de/2016/4493/4493.htm (cit. on p. 7).

[7] B. E. Reitz, *Coherent bremsstrahlung with the scintillating fiber detector of the BGO-OD tagging system*, URL: https://www.pi.uni-bonn.de/schmieden/medien/medien-ergebnisse (visited on 31/03/2023) (cit. on pp. 7, 11, 12, 14).

[8] S. Alef, *Scintillating fibre detector and kinematic fitting for the BGO-OD experiment*, URL: https://www.pi.uni-bonn.de/schmieden/medien/medien-ergebnisse (visited on 31/03/2023) (cit. on p. 7).

[9] R. Brun, F. Rademakers and S. Panacek, *ROOT, an object oriented data analysis framework*, (2000), URL: https://cds.cern.ch/record/491486 (cit. on p. 8).

[10] *Welcome to the BGOOD experiment - PI Uni Bonn Homepage*, URL: https://www.cb.uni-bonn.de/ (visited on 06/05/2023) (cit. on p. 8).

[11] 0. K.A. Olive et al. (Particle Data Group) Chin. Phys. C38, η, (2014), URL: URL:%20http://pdg.lbl.gov (cit. on p. 22).

[12] R. L. Workman et al., *Review of Particle Physics*, PTEP **2022** (2022) 083C01 (cit. on p. 22).

[13] O. Bartholomy et al., *Photoproduction of η -mesons off protons*, The European Physical Journal A **33** (2007) 133, ISSN: 1434-601X, URL: https://doi.org/10.1140/epja/i2007-10455-9 (cit. on p. 22).

[14] 0. R.L. Workmanet al.(Particle Data Group) Prog.Theor.Exp.Phys., *PDG Decay modes of light unflavored mesons*, (2022), URL: https://pdg.lbl.gov/2022/tables/contents_tables_mesons.html (cit. on p. 23).

[15] S. A. et al., *Geant4—a simulation toolkit*, Nuclear Instruments and Methods in Physics Research Section A: Accelerators, Spectrometers, Detectors and Associated Equipment **506** (2003) 250, ISSN: 0168-9002, URL: https://www.sciencedirect.com/science/article/pii/S0168900203013688 (cit. on p. 28).

[16] Anisovich, A. V. et al., *Photoproduction of baryons decaying into $N\pi$ and $N\eta$*, Eur. Phys. J. A **25** (2005) 427, URL: https://doi.org/10.1140/epja/i2005-10120-5 (cit. on p. 30).

List of Figures

List of Tables